

IMPROVED CORRELATION WITH THE HART-II ROTOR TEST DATA USING COUPLED CSD/CFD AND THREE LEVELS OF NUMERICAL MODELIZATION

Mathieu Amiriaux* James D. Baeder† Sudarshan N. Koushik‡

Department of Aerospace Engineering
University of Maryland, College Park, MD 20742, USA

This paper presents the application of coupled CSD/CFD methodologies to the HART-II rotor test. Three levels of aerodynamics modelization are implemented and compared. The first method is based on a simple lifting-line method, with modified compressible unsteady formulation to better predict the typical features of the HART-II flight condition, which is dominated by strong Blade-Vortex Interaction (BVI). The second method is a hybrid wake coupling approach which uses a body-fitted mesh to capture near-field flow and a free-wake module to preserve the far-wake vortical structures. Finally, a wake capturing method is used, in which multiple overset meshes capture the entire flow field. These three approaches each bring an additional level of numerical accuracy although their computational cost increases respectively. Each one is loosely coupled to a structural module which provides blade deformations and trim information. To further increase numerical correlation, improvements have been brought to each codes to better represent the flow field in this BVI dominated environment, creating a complete multi-fidelity framework for rotorcraft analysis.

1 MOTIVATION AND BACKGROUND

For the past 10 years, the HART-II rotor test and its extensive experimental dataset has been a major database for numerical validation of rotorcraft codes. Its low speed descending flight condition ($\mu = 0.15$, $\alpha = 5.3^\circ$ (corrected to 4.5° to account for wind tunnel effects), $M_{tip}=0.6387$, $C_T=0.00457$) sees strong Blade-Vortex Interaction (BVI) occur both on the advancing and retreating sides of the rotor disk, as the wake stays in the plane of the rotor. In fact, the strongest interactions occur for azimuths around 50° and 300° , where vortices are parallel to the leading edge of the blades. This leads to high levels of intrusive noise. Higher Harmonic Control (HHC) is used to lower noise and vibrations, through a precisely sized and phased 3/rev additional blade pitch input, leading to three different flight conditions: the Baseline (BL), Minimum Noise (MN), and Minimum Vibration (MV) cases. Their respective value of 3/rev HHC blade root pitch amplitude and phase are shown in

Table 1, along with the Baseline case (BL) which does not have HHC. The HART-II testing was carried out in 2001 at the German-Dutch Wind tunnel (DNW), following the 1994 HART-I campaign. Measurements included blade pressure, 3C-PIV (Particle Image Velocimetry), SPR (Stereo Pattern Recognition), BTD (Blade Tip Deflection), rotor balance, and noise levels, making the HART-II database one of the largest for rotorcraft, along with the UH-60A Airloads Program. More detail about the HART-II testing is given in [1]. As for numerical simulation, it seems that methods based on linearized aerodynamics and on the wake capturing approach have been extensively employed to predict the typical BVI condition of the HART-II rotor. The most up-to-date results from the different organizations taking part in the HART-II project using these two types of methods were published at AHS 2012 ([2] and [3]). The goal of this paper is to implement and compare these two levels of numerical modelization, along with another one: the so-called hybrid or wake coupling strategy, which has received less attention. In 2006, Gopalan et al published preliminary results from UMD, using the wake coupling approach with the Navier-Stokes solver Sumb (Stanford University Multi-Block) [15]. In the present paper, each method is loosely coupled to a Computational Structural Dynamics (CSD) code which provides blade deflections and control settings. Various improvements have been brought to each

*Ph.D. Student. E-mail: mamiriaux@umd.edu

†Associate Professor. E-mail: baeder@umd.edu

‡Research Associate. E-mail: nsud@umd.edu

Presented at the 38th European Rotorcraft Forum, Amsterdam, Netherlands, September 4–7, 2012. Copyright ©2012 by the authors except where noted. All rights reserved. Published by the ERF IC with permission.

Case	Amplitude	Phase
Baseline (BL)	0.0 °	0.0 °
Minimum Noise (MN)	0.81 °	300 °
Minimum Vibration (MV)	0.79 °	180 °

Table 1: 3/rev HHC blade root pitch amplitude and phase of the three cases.

module to better represent the influence on the flow field of the strong BVI.

2 COUPLING STRATEGY AND FRAMEWORK

As mentioned above, three levels of numerical simulation have been implemented in this multi-fidelity framework. First, a simple linearized unsteady aerodynamics solver based on the lifting line theory, coupled to a free-wake solver. Second is the wake coupling methodology using a RANS CFD solver for the near-field, and a free-wake module for the far-field. And third is the wake capturing method using the same RANS solver over the entire computational domain. The linearized aerodynamics module is used as an external module and coupled to the other codes using the “delta coupling” method, despite the fact that the CSD comprehensive module has its own aerodynamics solver, with a uniform inflow assumption. The reason behind this choice was to be able to easily bring modifications to the aerodynamics modeling, to use an accurate free-wake modeling with time marching, a finer time step size in azimuth, and a better unsteady model. The simpler aerodynamics model present in the CSD code and its larger time step of 5 ° is sufficient to obtain the lower frequency airloads necessary for accurate structural deformations predictions and to perform trim, at a reduced numerical cost. The loose coupling method developed by Tung, Caradonna, and Johnson [4] is used between the CSD code and the different aerodynamics solvers. This means that data is only exchanged at every rotor revolution, unlike the tight coupling approach in which data is transferred after every time step. The initial CSD solution uses linearized aerodynamics with uniform inflow to obtain the trimmed blade deflections and control angles. This data is then sent to either aerodynamics solvers and several rotor revolutions are performed to obtain a periodic solution. For the CFD solvers, the blade grids are deformed to reflect these deflections. The resulting airloads are transferred back to the CSD code through “delta coupling”: after every rotor revolutions, delta values of normal force, chord force, and pitching moments are computed as the difference between the CFD and Lifting-Line (from CSD) airloads. This difference is applied to the CSD airloads to obtain new trimmed blade deformations and control angles. This coupling cycle goes on until a converged solution is reached. Table 2 shows the number of coupling cycles performed for each of the three levels of modelization, as well as the

Iteration number	Linearized Aerodynamics	Wake Coupling	Wake Capturing
1	5 revs	360 °	1080 °
2	5 revs	270 °	720 °
3	5 revs	180 °	360 °
4	5 revs	180 °	180 °
5	5 revs	180 °	180 °
6	-	180 °	180 °
7	-	180 °	180 °
Run-time	2 hours	1 week	3 weeks

Table 2: Coupling cycles required by the different solvers.

number of degrees of azimuth each solver is run for each coupling cycle. The linearized aerodynamics only takes 5 coupling cycles whereas wake coupling and wake capturing run for 7. For the CFD based methods, the airloads are obtained by keeping the last 90 ° of solution from each blade and splicing them together. It should be noted that the wake capturing method requires more rotor revolutions to be performed within each cycle, especially for the first few cycles as the wake needs to develop and settle in the computational domain, keeping in mind that the most intense BVI interaction occurs for wake ages close to two rotor revolutions. Table 2 also shows the average total run-time of each code using 32 3.2 GHz Intel Xeon cores for the CFD based methods and 4 cores for linearized aerodynamics. Clearly, the wake capturing method takes the longest time to run, with the linearized aerodynamics based method being the fastest, which is very useful for code debugging and testing purposes, while still maintaining satisfactory levels of accuracy (as shown below and in [2]). Figure 1 shows the interaction between the codes and the three different aerodynamics solvers, using the “delta coupling” approach discussed above.

3 CODES DESCRIPTIONS

The following section describes the different codes mentioned above and their numerical implementations. In their 2008 paper, Ananthan et al. described the HUSH framework in detail [5], from which this work is based on.

3.1 Structural dynamics solver: UMARC

The comprehensive aero-elastic analysis is based on a finite element methodology [6]. The four blades are modeled as second order non-linear isotropic Euler-Bernoulli beams. They are divided into 20 span-wise elements undergoing coupled flap, lag, torsion, and axial degrees of freedom based on [7] and [8], resulting in a total of 15 degrees of freedom for each beam element. Modal reduction is limited to the first 10 dominant natural modes (5 flap, 3 lag, 2 torsion). The structural dynamics equations are integrated in time using the finite element in time procedure which uses 12 equal temporal elements, with 6 points within each element. This results in an effective azimuthal

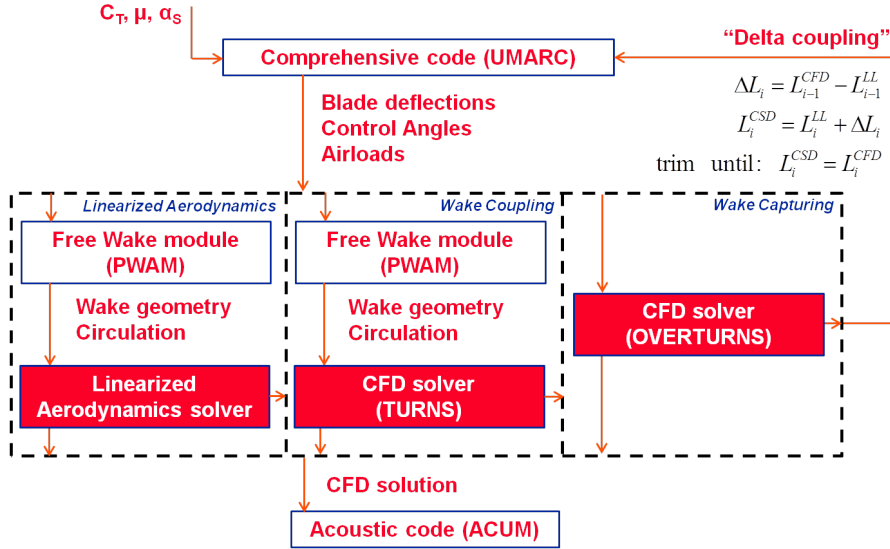


Fig. 1: Interaction between the different codes using the “delta coupling” approach.

discretization of 5° . Rotor trim is performed to the target thrust and hub roll/pitch moments obtained from wind tunnel measurements. A free-flight propulsive trim algorithm is used [9]. The force summation method is used to compute the bending moments. As mentioned above, UMARC has its own linearized aerodynamics solver which, for these results, uses a uniform inflow assumption. Iteration histories for the different trim angles (θ_0 , θ_{1C} , θ_{1S}) are plotted in Fig. 2 and show good converge after a few coupling cycles.

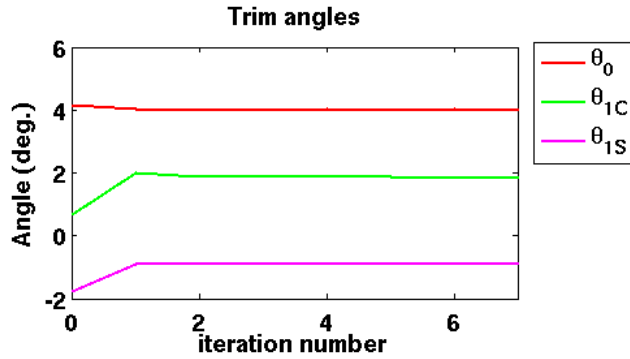


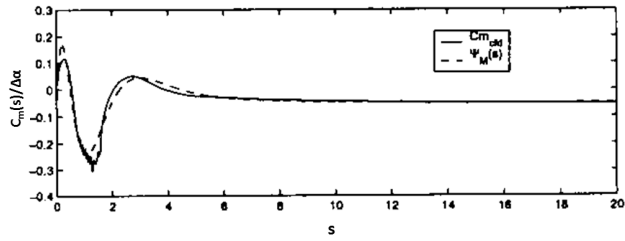
Fig. 2: Iteration histories of the trim angles (BL case, wake coupling method).

3.2 Aerodynamics solvers

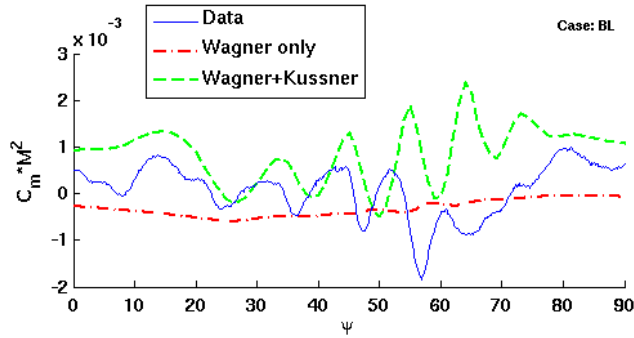
3.2.1 Lifting-line linearized unsteady aerodynamics

A multi-bladed lifting-line linearized compressible unsteady aerodynamics model is used. The sectional blade lift, drag, and moment coefficients are obtained using two-dimensional airfoil lookup tables. In addition, the

Weissinger-L near-wake model [10] and the Leishman-Beddoes two-dimensional unsteady aerodynamic model [11] are used. The azimuthal discretization is 1° with 120 spanwise elements. The nearwake region spans over 30° . Modifications were made to the indicial model to better represent the specific case at hand. Unsteady computations used to be based on the Wagner compressible indicial modeling, which brings unsteady effects to the solution through step changes in angle of attack and pitch rate and their time histories. However, for the HART-II case, a major contribution to the changing angle of attacks and pitch rates come from the strong vertical gusts that appear in the vicinity of each blade, due to the passing vortices. Therefore, it was decided to modify the indicial modeling, keeping the compressible Wagner formulation to compute the unsteady effects due to the rotor kinematics, and adding a compressible Kussner formulation for the unsteadiness due to the inflow. This unsteady modeling can be critical for accurate airloads predictions, especially for the pitching moments. A generalized moving gust function was developed by Sitaraman et al [23] and the various required constants were derived from CFD simulations. As can be seen in Fig. 3(a), which shows the Kussner function and the generalized moving gust function for pitching moments plotted versus time in semi-chord, although the values are close to zero for the smallest times and go to zero for higher times, it can be seen that a significant portion is non-zero with a large negative peak. This has a big impact on the pitching moments, as shown in Fig. 3(b) where $C_m M^2$ predictions using both formulations are compared to experimental values on the advancing side. It is clear that the hybrid Wagner-Kussner formulation does a better job of capturing the high frequency content due to BVI events.



(a) Pitching moment response due to Kussner.



(b) Pitching moment predictions

Fig. 3: Influence of the indicial model on the pitching moments.

3.2.2 CFD modules: TURNS

The University of Maryland Transonic Unsteady Reynolds-averaged Navier Stokes (TURNS) [12] code is an unsteady RANS solver. It uses a second-order backward difference method using Lower-Upper Symmetric Gauss Seidel (LUSGS) [13] for time integration with dual time-stepping. By default, six Newton sub-iterations are used to remove factorization errors and recover time accuracy for unsteady computations [14]. The inviscid fluxes are computed using a third order upwind scheme that uses Roes flux differencing with MUSCL type limiting. The viscous fluxes are computed using second-order central differencing. The Baldwin-Lomax turbulence model is utilized for RANS closure (since flow is attached). The solver uses four identical body-fitted C-O meshes consisting of 129 points in the wraparound direction (of which 97 points are on the blade surface), 129 points in the spanwise direction, and 65 points in the normal direction, which extend up to 3 chords at 70% radius. Clustering is applied at the tip and root of the blade, as well as near the leading and trailing edges and in the normal direction. The value of y^+ is kept to 1.0 with 20 to 30 points inside the boundary layer at 70%R, with a spacing at the wall of $10^{-5}c$, to accurately capture the wall-bounded viscous effects.

Figure 4 shows the different spanwise discretizations used by the different codes. While all use almost the same number of points (129 for CFD, 120 for the structural solver and linearized aerodynamics), different levels of clustering

are applied. As expected, the structural solver has a refined distribution near the root to better capture the blade structural deformations. The CFD solver has refinement both at the root and at the tip to help preserve the forming vortical structures. However, the linearized aerodynamics solvers has a uniform spanwise distribution of points.

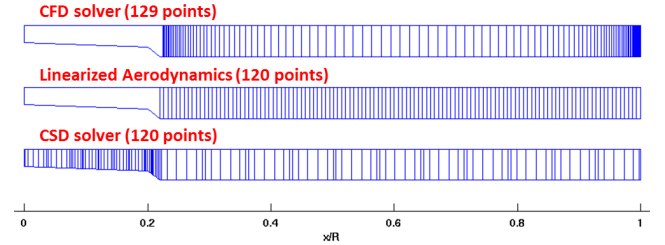


Fig. 4: Spanwise distributions used by the different solvers.

3.3 Far-field modelization

3.3.1 Free-wake module: PWAM

In the wake coupling approach, the effects of the far-field are prescribed using a free-wake solver and the field-velocity method, in which velocities induced by vortex filaments are computed at each grid points, using the Biot-Savart law, and added to the grid velocities. The free-wake module, PWAM (Parallel Wake Analysis Module) developed at the University of Maryland is a time accurate, efficient, scalable parallel implementation of the solution of the vorticity transport equations in a Lagrangian domain [15]. The wake geometry is discretized into vortex filaments whose strengths are calculated from the provided aerodynamic forcing. The convection velocity of each vortex filament is computed by aggregating their mutual influences and the free stream convection velocity. The mutual influence between the vortex filaments can be computed using the Biot-Savart law. The resulting equations for wake positions are integrated in time using a second order Runge-Kutta scheme. The wake azimuthal discretization (temporal) is 0.25° while a 5° discretization is used in wake age (spatial). In the meantime, the first filament is allowed to grow to its full size before being released. This reduces the computational cost significantly. The trailed vortex system consists of a root vortex and a tip vortex which convect for three revolutions. To account for the possibility of negative lift across the rotor disk and generation of two counter rotating vortices, the tip vortex release point is allowed to move to the first spanwise point of negative lift in the outer portion of the blade. The spanwise direction is discretized using 20 elements. The near wake region also spans over 30° before rolling up into a tip vortex, whose strength is the maximum blade bound circulation found in the outer

half of the blade. Vortex aging follows Squire’s law [20] and the swirl velocity model is due to Scully’s formulation, see [21]. Figure 5 shows the computational domain used for the wake coupling methodology. The free-wake filaments are represented with their actual core radii. It should be noted that the two boxes shown are only displayed to give a size comparison with the computational domain used in the wake capturing approach.

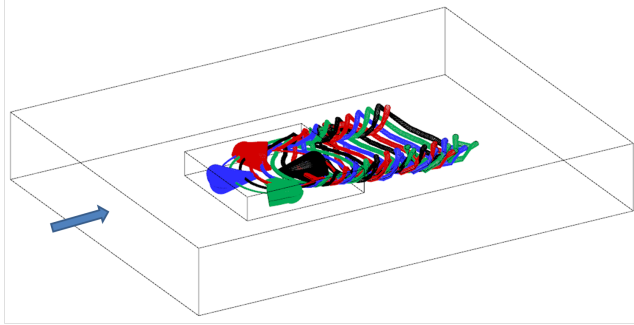


Fig. 5: Computational domain of the wake coupling methodology.

3.3.2 Off-body CFD solver

The wake capturing approach uses multiple overset rectangular Cartesian meshes for the far-field, each level of grid having a different spacing and adequate stretching between them. Although this methodology is much more computationally expensive than the previous two, it usually shows the highest level of accuracy and correlation with experimental data. OVERTURNS is the version of TURNS designed for overset grid topologies. An implicit hole cutting (IHC) strategy [16] is used to determine connectivity between the different overlapping grids. In the present work, 2 levels of cartesian background meshes are used. The finer level consists of a mesh with a spacing of 0.1 chords and extending 1.1R in front of the rotor and 1.5R behind, 1.2R on each side, and 0.25R above and below the rotor. The spacing extends up to 0.8 chords in an overlap region with the coarser background mesh. This second mesh extends up to 6 rotor radii behind the rotor, 3.5R in front and on each side, and 0.7R above and below. It has a spacing of 0.8 chords extending up to 1.6 chords at the far-field boundary. The total number of grid points is 13.5 million. Figure 6 shows this computational domain. The same body-fitted grids as described above are used to capture the near-field in this approach. Using this setup, it was noticed that it was difficult to correctly capture and preserve the vortical structures present in the flow field as the necessary grid spacing to avoid numerical dissipation would drive the computational cost too high for the available resources. Therefore, it was decided to use a higher order scheme for spatial discretization of the inviscid terms, namely a fifth order Weighted Es-

Grid	Type	Points	Spacing (finest)
Blade (1)	Structured, curvilinear	1.08M	$10^{-3}c$
First background	Structured, cartesian	8.5M	0.1c
Second background	Structured, cartesian	0.8M	0.8c

Table 3: Computational grids details (wake capturing).

entially Non-Oscillatory (WENO). This scheme was used only on the finer background grid, while all other grids used the third order scheme described above. Figure 7 shows the relative spacing used by the blade meshes and the finer level of cartesian background grid. Table 3 summarizes the types and sizes of the different grids that are used in this study for wake capturing.

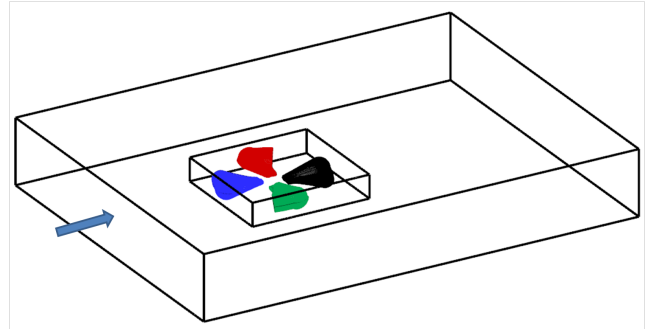


Fig. 6: Computational domain of the wake capturing methodology.

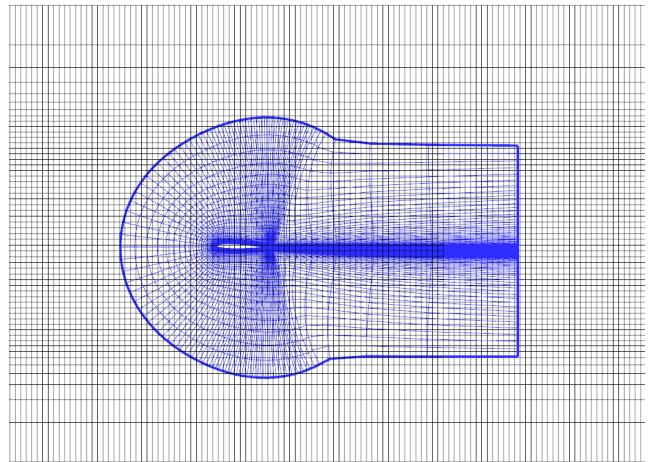


Fig. 7: Visualization of one of the blade grids and the finer level of background mesh.

3.4 Noise radiation computation: UMAC

The acoustics code developed at the University of Maryland is based on the Ffowcs Williams and Hawkins [17] equations and is capable of both on- surface and off-surface computations using Formulation 1A [18]. Pressures, velocities and density from TURNS are used for the off-

surface (permeable surface) acoustics computation, while blade surface pressures alone are used for the on-surface (impermeable surface) acoustic computations. The acoustics code can also compute the near and far-field radiated noise using integrated lift and drag prescribed on the blade surface. This code has been extensively validated against BVI experiments performed at the University [19].

3.5 Python coupling

This coupling approach between the various solvers is implemented using Python scripts. For each solver, a Python class interface is created, which interacts with the Fortran modules using Fortran to Python Interface generator (F2PY). Parallelization of the code is achieved using pyMPI. The different computational grids are split into blocks to achieve near load-balanced simulations. The Python NumPy library is used for array manipulation and data exchange between the solvers. While UMARC is used for the structural model in this analysis, the framework is generic enough to incorporate an alternate structural solver. Data from the different codes is interpolated using spectral interpolation in azimuth and cubic spline interpolation in the radial direction, according to the different discretizations used.

4 PARAMETRIC STUDIES

4.1 Linearized aerodynamics: optimal time step for accurate BVI prediction

The influence of the time step size was determined by running the linearized aerodynamics code with different time step sizes, ranging from 5.0° to 0.25° . This study was to determine the minimum time step required to capture the BVI events as accurately and efficiently as possible. Figure 8 shows the normal force and pitching moment coefficients, as well as their time derivatives as a function of azimuth on the advancing side for the baseline case. It can be seen that for a time step above 2.5° , the sharp BVI peaks are not well captured in magnitude because not enough points in the azimuthal direction are being used. However, the low frequency is satisfactory. For a time step of 1.0° , which is what was used for the rest of this study, the difference with the two lowest values of $d\psi$ is minimal, as only a small fraction of the magnitude is missing for the sharpest peaks. This time step size also saves on computational cost. The structural deformations and loads are not affected by the value of $d\psi$ used in the aerodynamics solver, as only the lower frequency content of the airloads is of importance. This is why the time step size used in the structural solver was only 5.0° .

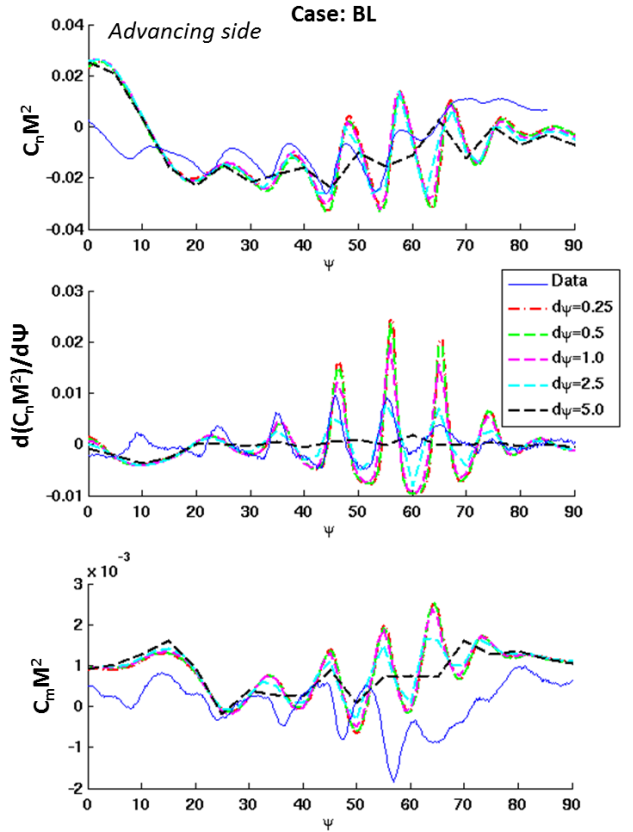


Fig. 8: Influence of the time step size on BVI peaks predictions.

4.2 Linearized aerodynamics: wake modelization (root/tip vortex, wake age, number of trailers)

The influence of the vortex modelization in the free-wake module was also assessed. The inclusion of root vortices in addition to those released at the tip of the blade and the number of revolutions each vortex is free to convect for was varied. Two and three revolutions were considered as nearly all BVI events occur for wake ages lower than two rotor revolutions. Figure 9 shows the impact on the normal force. While adding root vortices in the simulation made an important difference, the number of revolutions only had a minor influence. Although no difference is seen in terms of phase, the magnitude of the BVI peaks is different whether root vortices are present or not, at least on the advancing side. When present, the normal force derivatives are always over-predicted. This is the case only for later azimuthal location when both vortices are included. At the front of the rotor, a large difference can be seen between the two representations, with the one without the root vortex under-predicting the peak-to-peak magnitude. It should also be noted that the retreating side is not affected as much, as well as the pitching moments. The blade deflections are mildly affected by these parameters, with both vortices modelled and more revolutions being slightly beneficial (not shown).

This parametric study was also useful for the wake coupling methodology as the free-wake module used was the same. The fact that the linearized aerodynamics based approach runs much faster than the wake coupling method made it easier to conduct. Further studies should be carried out to determine the optimal initial core radii and vortex growth rates for both the tip and root vortices, along with vortex strength, the idea being to get as close as possible to the levels of swirl velocities seen in experimental PIV maps.

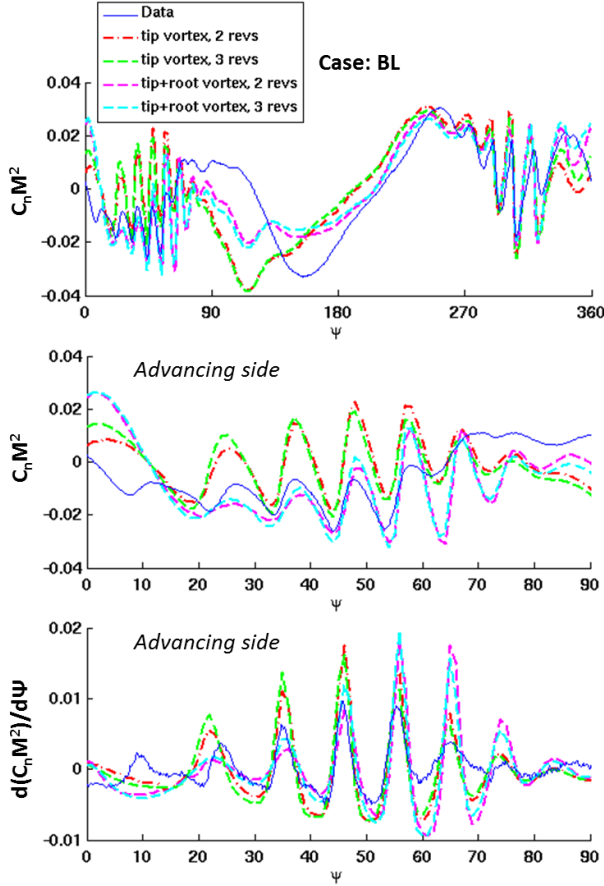


Fig. 9: Influence of the vortex modelization.

Finally, the number of trailers used in the near-wake model was varied from 20 to 120. Figure 10 clearly shows that this parameter does not have an impact on airloads predictions as they are very similar to each other. A study of the influence of the number of trailers in the far-wake model should be carried out, although such analysis has already been conducted by Lim et al. [24], which showed that more trailers was beneficial for airloads predictions.

4.3 Wake coupling: number of sub-iterations and time step size

Early numerical simulations using the wake coupling approach showed large overpredictions of BVI peaks in the

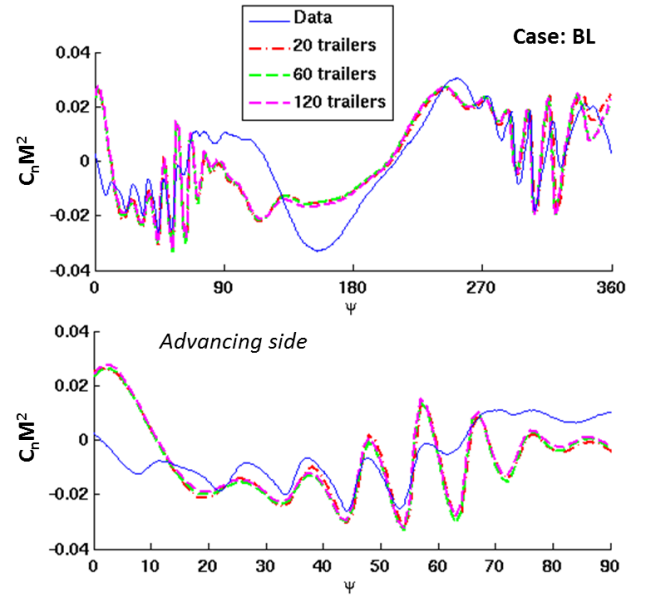


Fig. 10: Influence of the number of trailers in the near-wake.

pitching moments, especially for the minimum vibration case. It was determined that this was due to the relatively low number of sub-iterations used, six, and that more sub-iterations were required to better resolve the pitching moments and obtain more convergence within every time step. Further testing was done using 10 and 15 sub-iterations and the impact on $C_m M^2$ is shown in Fig. 11. The influence of the time step size on this issue was also examined, going from 0.25° to 0.125° with 10 sub-iterations. It can be seen that with more sub-iterations, the over-prediction of the pitching moment decreases. Going to a smaller time step size of 0.125° with 10 sub-iterations, which is equivalent to running 20 sub-iterations at 0.25° , does not present any clear improvement compared to 15 sub-iterations at the larger time step. In addition, no real difference was noticed in the normal force. Therefore, 15 sub-iterations were used in this study with $d\psi = 0.25$.

5 RESULTS

The three methodologies described above have been applied to the HART-II baseline condition as well as the minimum noise and the minimum vibration cases, which include 3/rev higher harmonic blade pitch control. Comparison is made with experimental measurements. The data presented includes normal force and pitching moment coefficients at 87% span, blade tip flap, lead-lag, and torsion deflections as well as the related bending moments, control angles, wake geometry, and finally noise radiation.

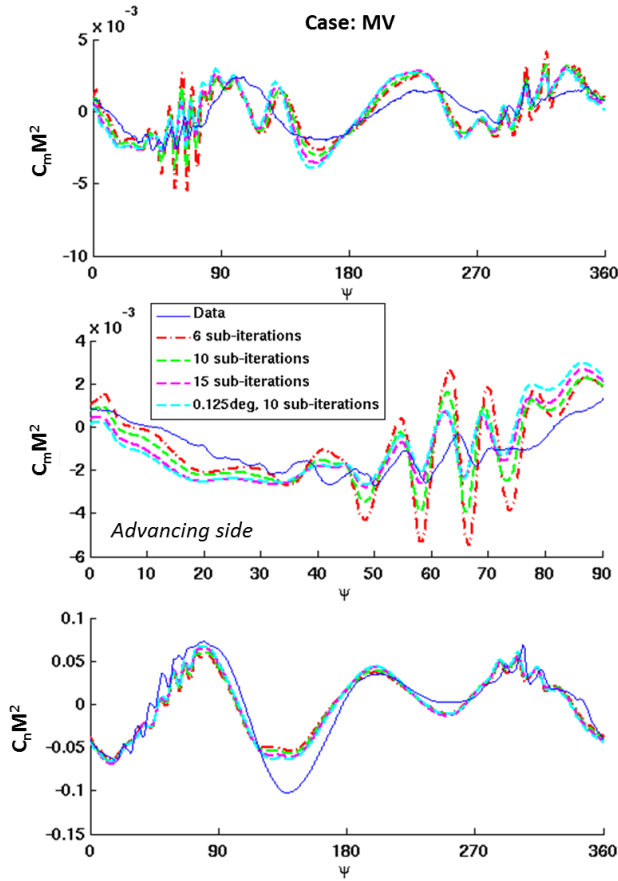


Fig. 11: Influence of the number of sub-iterations on the pitching moments.

5.1 Airloads

Predictions of normal force and pitching moment coefficients are compared with those from experiment at the 87%R spanwise location. It should be noted that all airloads are plotted with mean removed. The mean values plotted in Fig. 12 show good agreement with the experimental data, except for the MN and MV pitching moment but the experimental values are thought to be offset [2]. It can be seen in Fig. 13 that all three methods capture the low frequency content of the normal force correctly, although only the CFD based approaches manage to predict the full peak-to-peak magnitude near the front of the rotor disk. The MN and MV cases display a strong 3/rev behavior due to HHC, which can also be seen in the structural deformations and moments (flap and torsion). For the baseline case, it can be seen that the phase of the lower peak near 180° is offset by a few degrees by all three methods. This could be due to the fact that no fuselage model was included in this study, as recent studies [25 - 26] showed that such a model made an important difference at the front and back of the rotor. The pitching moment trend is well captured by both CFD methods (Fig. 14), while linearized

aerodynamics proves quite satisfactory, thanks to the hybrid Wagner-Kussner unsteady formulation used. The wake coupling approach predicts a large oscillation in the pitching moment near 100°, both in the BL and MN cases. It is assumed to be due to the free-wake modelization and needs further investigation. Figures 15, 16, and 17 are close-up views of the advancing and retreating sides of the normal force and pitching moment, for the BL, MN, and MV cases. The unfiltered data is shown along with the 10/rev filtered data and time derivatives. These views allow easy comparison of BVI loading predictions. The linearized aerodynamics based method over-predicts the magnitude of the peaks due to BVI on the advancing side, while the wake coupling approach seems quite reasonable. However, the wake capturing method does not give adequate BVI predictions on the advancing side as the peaks are clearly under-predicted, the retreating side peaks being better captured. This is due to the fact that the vortices responsible for the BVI peaks on the advancing side are older than on the retreating side and therefore, are more diffused at the time of interaction. This suggests that a finer grid resolution might be necessary on the first level background mesh (going from 0.1c to 0.05c) to better preserve those structures. It should also be noticed that both free-wake based methods show the largest BVI peak at later azimuths than the experimental data, although the phasing of each peak is quite good. This can be explained by the lower vertical position of the filaments which lead to later interactions with the blades, as will be seen in the wake geometry comparison. Despite being under-predicted, the largest BVI peak predicted by the wake capturing approach seems in phase with the data. Compared to the BL case, the MN case shows lesser and smaller BVI events on the advancing side and those are shifted upstream, near the 70° azimuthal location, due to the application of HHC. This results in lower levels of noise. All methods display this trend but are unable to capture the large peak near 70°. The pitching moment predictions of the peaks due to BVI are much less satisfactory in terms of phase, magnitude, and occurrence. Both free-wake based approaches shows some over-prediction on the advancing side, although the use of more sub-iterations in the wake coupling approach made these levels acceptable. Overall, the wake coupling approach shows the best level of correlation, but a finer grid resolution would allow the wake capturing method to predict the BVI events more accurately (as seen by others [3]). Considering the much shorter run-time required by the linearized aerodynamics, its level of accuracy is very encouraging.

5.2 Blade Elastic Motion

Blade tip deflections including elastic flapping, lead-lag, and torsion are plotted in Fig. 18 for the different methods versus experimental data. The experimental bands show

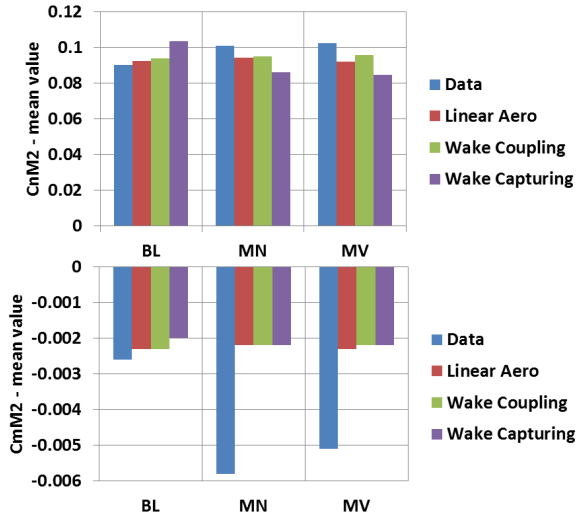


Fig. 12: Normal force and pitching moment, mean values.

that significant dissimilarities were measured between the blades. Flapping motion is plotted without displacement due to precone. Lead-lag motion is shown with mean removed, as the experimental mean levels are thought to be offset. Finally, blade torsion is plotted without pitch due to control angles and higher harmonic control, as well as the linear built-in blade twist. It can be seen that both free-wake based methods under-predict the flapping displacement at the front of the rotor while the wake capturing approach is close to the experimental data. The lead-lag motion is well predicted by all methods, although the linearized aerodynamics approach displays a slight phase shift of the peak, which is thought to be due to the lack of unsteady modeling of the rotor drag. The elastic twist predictions of the CFD based methods for the BL case have an additional oscillation on the advancing side, especially large for the wake capturing approach, which needs further investigation. For the MN and MV cases, the strong 3/rev elastic pitching motion can be observed. Both CFD based methods are capturing the peak-to-peak magnitudes correctly but the linearized aerodynamics method often under-predicts these oscillations. Overall, the wake capturing approach gives the best levels of correlation with the experimental data, despite lacking correct BVI airloads predictions. But this loading is of higher frequency which has little impact on the structural behavior of the rotor blade.

5.3 Rotor Trim

Rotor trimmed control angles (θ_0 , θ_{1C} , θ_{1S}) are plotted in Fig. 19 for all three cases. It can be seen that the wake coupling approach gives better predictions than the other two methods, although the offset is usually less than 0.5° . The

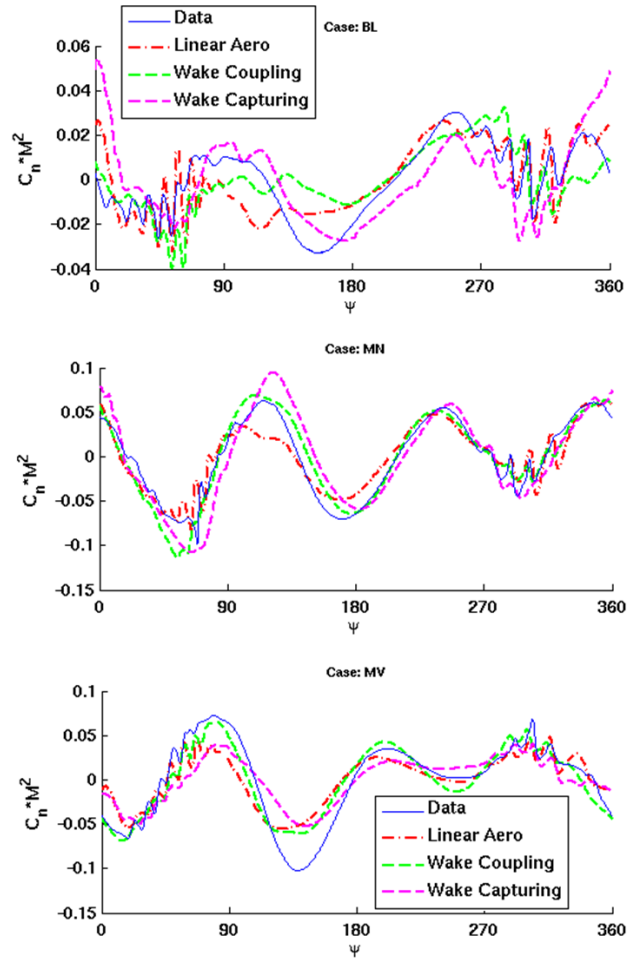


Fig. 13: Normal force, unfiltered data, BL, MN, MV cases.

longitudinal cyclic pitch (θ_{1S}) is slightly under-estimated by both CFD based methods [2] while it is over-predicted by the linearized aerodynamics.

5.4 Blade Structural Moments

Blade structural moments have proven difficult to accurately predict as a large scatter was observed in [2] and [3] between different state-of-the-art structural solvers. Shown here are the bending moments in flap (at 17%R), lag (at 17%R), and torsion (at 33%R) using the force summation method. All simulations give satisfactory results in flap. The lag bending moment predicted by the linearized aerodynamics method is slightly offset in phase, as seen in the tip lead-lag results. The higher frequency content present in the data is captured by all methods, although the wake capturing does over-predict these oscillations. The torsion moments are in somewhat good agreement with the experimental data for both CFD based methods, but is under-estimated by the linearized aerodynamics.

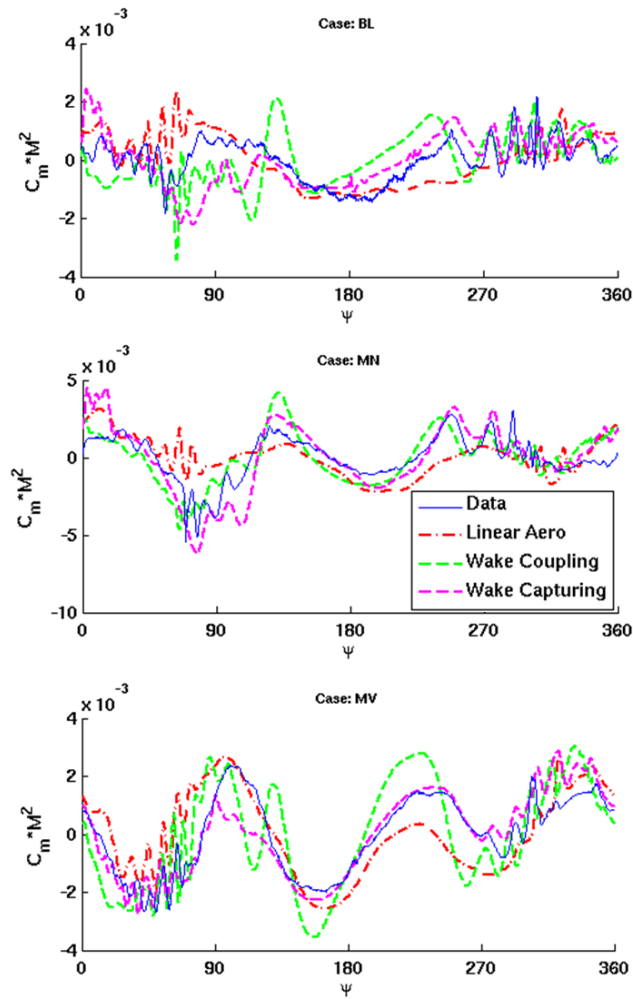


Fig. 14: Pitching moment, unfiltered data, BL, MN, MV cases.

5.5 Wake Geometry

Iso-surfaces of Q-criterion are shown in Fig. 21 for the MV case, colored by vorticity magnitude with levels going from 0.03 to 0.15. Experimental vortex center locations are known in two lateral planes on the advancing and retreating sides at $\pm 70\%R$, as shown in Fig. 22. This data was obtained with the reference blade at two azimuthal locations: 20° and 70° . Predictions at those two planes using all three methods are compared in Fig. 23 for the BL (a), MN (b), and MV (c) cases. It can be seen that the wake capturing method is the closest to the experimental data, although the wake coupling approach gives reasonable results, especially at the back of the rotor where the wake capturing method predicts a higher wake position. This is probably due to the fact that the intermediate vortices (older vortices near the center of the rotor) that should push the vortex system down are somewhat diffused. The linearized aerodynamics gives the poorest prediction with a lower overall wake posi-

tion. It should be noted that both free-wake based methods have similar wake locations in the first quarter of the rotor disk, which, as seen previously, leads to an offset of the BVI peak of maximum magnitude, as the blades hit the vortices later. The experimental results for the MV case show a dual-vortex system on the advancing side. This is due to a negative tip loading around azimuths of 150° and the formation of a counter-rotating vortex. However, both free-wake based methods do not capture this phenomena as no negative loading is predicted. The wake capturing method was able to predict the higher wake locations on the advancing side but the counter-rotating vortex could not be extracted (Fig. 22). This clearly shows that a refinement of the free-wake model is necessary, as well as a finer discretization for the wake capturing approach.

5.6 Noise Levels

Sound Pressure Level (SPL) contours were obtained experimentally from a microphone array placed $1.1R$ below the hub, and extending $2R$ in front and behind and $1.35R$ on each side on the rotor. BVISPL (6-40 Blade Passage Frequency (BPF) filtered) for this noise carpet are compared with numerical results in Fig. 24. It should be noted that SPL are mostly influenced by airloads time derivatives. It can be seen that, as expected due to the larger time derivatives of BVI loading, the linearized aerodynamics based method gives over-predicted levels. However, the wake coupling approach seems to give satisfactory noise levels and all methods predict the right directivity pattern: in the MN case, the advancing side hot-spot is shifted upstream and reduced in intensity, in the MV case, the hot-spot is larger and stronger. In addition, the dual hot-spot that appears in the MN case is only predicted by the wake coupling. Acoustic results for the wake capturing approach are not shown here as most BVI events were noticeably smaller than experimental data, leading to low time derivatives and greatly under-estimated noise levels.

6 CONCLUSION

This paper presented the application of a multi-fidelity coupled CFD/CSD framework to the HART-II rotor test. Three levels of aerodynamics modelizations were used and compared to experimental data.

- The method based on a linearized aerodynamics model proved quite accurate considering its low required runtime. Airloads were somewhat over-predicted, leading to higher noise levels. The pitching moments benefited greatly from the hybrid Wagner-Kussner unsteady formulation.

- The wake capturing method and the level of numerical refinement used generated unsatisfactory results. BVI events were largely under-predicted on the advancing side, leading to lower noise levels. The BVI induced airloads were fairly reasonably captured on the retreating side and it is expected that an additional level of refinement to 0.05c would allow for reasonable capture of the BVI airloads on the advancing side. The structural deformations and moments showed good comparison with experimental data, as the lower frequency content of the airloads was accurately predicted.
- The wake coupling approach proved to give the highest level of correlation, although some discrepancies due to the free-wake model, which still needs refinement, were observed. In that regard, the wake capturing approach showed encouraging results as the BVI events phasing and wake geometry were closer to experiments.

7 RECOMMENDATIONS

- The free-wake modelling should be refined to give better BVI predictions. The influence of the vortex core size and strength need to be investigated and compared to experimental PIV maps.
- The wake coupling approach could be modified to include a characteristic boundary condition instead of the field velocity method for calculating the effect of vortices on the grid points. This avoids the computation of the Biot-Savart law at every grid point, which can be expensive if not using a Fast Multipole Method (FMM). Grid velocities will only be modified at the mesh boundary, along with density, using isentropic relations, and pressure, using Bernoulli's principle. The vortices will then be free to convect inside the computational domain.
- As the wind tunnel testing was conducted using a generic fuselage and as recent studies [25 - 26] showed that a fuselage model could lead to higher levels of accuracy in BVI loading, the influence of a fuselage on the rotor and its surrounding flow field should be included in the further studies. For the two free-wake based methods, it can be added through the use of panel code for the generic HART fuselage. For the wake capturing method, it can be done using an immersed boundary condition where the fuselage shape is embedded inside a rectangular cartesian mesh using a hole cutting algorithm. A no penetration and no slip condition is enforced at the boundary and applied to the primitive variables through tri-linear interpolation.
- The level of grid refinement used in the wake capturing approach should be increased. The use of Vortex

Tracking Grids (VTG) can be considered, if the finer grid discretization required drives the numerical cost too high for the available resources.

- Airloads predictions could potentially be improved by integrating the chordwise pressure distribution at the 87% span location only where pressure sensors were positioned in the experiments. Good levels of improvement can be expected from such a method, especially for pitching moments, as shown by Biedron et al. [27] for the UH-60 and by Park et al. [28] for the HART-II rotor.

8 ACKNOWLEDGEMENTS

The authors wish to thank Sebastian Thomas, Ph.D. candidate at University of Maryland, for helping with the free-wake modelization and setting up the coupling between the different solvers.

9 REFERENCES

- [1]van der Wall, B.G., Burley, C.L., Yu, Y.H., Pengel, K., Beaumier, P., *The HART II Test - Measurement of Helicopter Rotor Wakes*, Aerospace Science and Technology, Vol. 8, (4), June 2004, pp. 273-284.
- [2]van der Wall, B. G., Lim, J. W., Smith, M. J., Jung, S. N., Bailly, J., Baeder, J. D., and Boyd, Jr., D. D., *An Assessment of Comprehensive Code Prediction State-of-the-Art Using the HART II International Workshop Data*, Presented at the 68th Annual AHS Forum, Fort Worth, TX, USA, May 1-3 2012.
- [3]Smith, M. J., Lim, J. W., van der Wall, B. G., Baeder, J. D., Biedron, R., Boyd, Jr., D. D., Jayaraman, B., Jung, S. N., and Min, B.-Y., *An Assessment of CFD/CSD Prediction State-of-the-Art Using the HART II International Workshop Data*, Presented at the 68th Annual AHS Forum, Fort Worth, TX, USA, May 1-3 2012.
- [4]Tung, C., Caradonna, F. X., and Johnson, W. R., *The Prediction of Transonic Flows on an Advancing Rotor*, Presented at the American Helicopter Society 40th Annual Forum, Arlington, VA, USA, May 1984.
- [5]Ananthan, S., Baeder, J. D., and Sitaraman, J., *Hybrid Unsteady Simulation of Helicopters: HUSH*, Presented at the 26th AIAA Applied Aerodynamics Conference, Honolulu, HI, USA, August 2008.
- [6]Chopra, I., and Bir, G., *University of Maryland Advanced Rotor Code: UMARC*, American Helicopter Society Aeromechanics Specialists Conference, San Francisco, CA, USA, January 1994.

- [7]Hodges, D.H., and Dowell, E. H., *Nonlinear Equations of Motion for the Elastic Bending and Torsion of Twisted Nonuniform Rotor Blades*, NASA TN D7818.
- [8]Ormiston, R. A., Hodges, D. H., and Peters, D. A., *On the Nonlinear Deformation Geometry of Euler-Bernoulli Beams*, NASA Technical Paper 1566.
- [9]Datta, A., *Understanding, Prediction and Validation of Rotor Vibratory Loads in Steady Level Flight*, Doctoral Dissertation, University of Maryland, MD, USA, 2004.
- [10]Weissinger, J., *The Lift Distribution of Swept-Back Wings*, NACA TM 1120, 1947.
- [11]Leishman, J. G., Beddoes, T. S., *A Semi-Empirical Model for Dynamic Stall*, Journal of the American Helicopter Society, Vol. 34, No. 3, July 1989, pp. 3-17.
- [12]Sitaraman, J., Baeder, J., and Chopra, I., *Validation of UH-60 Rotor Blade Aerodynamic Characteristics Using CFD*, Presented at the 59th Annual Forum of the American Helicopter Society International, Phoenix, AZ, USA, May 2003.
- [13]Yoon, S., and Jameson, A., *Lower-Upper Symmetric-Gauss-Seidel Method for Euler and Navier-Stokes equations*, AIAA Journal, Vol. 26, 1988, pp. 1025-1026.
- [14]Pulliam, T., *Time Accuracy and the use of Implicit Methods*, American Institute of Aeronautics and Astronautics 1993-3360, 1993.
- [15]Gopalan, G., Sitaraman, J., Baeder, J. D. and Schmitz, F., H., *Aerodynamic and Aeroacoustic Prediction Methodologies With Application to the HART-II Model Rotor*, Presented at the 62nd Forum of the American Helicopter Society, Phoenix, Arizona, USA, May 9-11, 2006.
- [16]Lee, Y., and Baeder, J. D., *Implicit Hole Cutting - A New Approach to Overset Grid Connectivity*, Presented at the 16th AIAA Computational Fluid Dynamics Conference, Orlando, FL, USA, June 2003.
- [17]Ffowcs Williams, J. E. and Hawkins, D. L., *Sound Generated by Turbulence and Surfaces in Arbitrary Motion*, Philosophical Transactions of the Royal Society, Series A, Vol. 264, 1969, pp. 321-342.
- [18]Farassat, F., *Linear Acoustic Formulas for Calculation of Rotating Blade Noise*, Journal of the American Institute of Aeronautics and Astronautics, Vol. 19, No. 9, September 1981, pp. 1122-1130.
- [19]Koushik, S. and Schmitz, F.H., *Understanding In-Plane Helicopter Blade-Vortex Interaction (BVI) Noise*, Presented at the 68th Forum of the American Helicopter Society, Fort Worth, TX, USA, May 2012.
- [20]Leishman, J. G., Bhagwat, M. J. and Ananthan, S., *Free-Vortex Wake Predictions of the Vortex Ring State for Single-Rotor and Multi-Rotor Configurations*, Presented at the 58th Forum of the American Helicopter Society, Montreal, Canada, June 2002.
- [21]Bhagwat, M. J., Leishman, J. G., *Generalized Viscous Vortex Model for Application to Free-Vortex Wake and Aeroacoustic Calculations*, Presented at the 58th Forum of the American Helicopter Society, Montreal, Canada, June 2002.
- [22]Chen, P., Baeder, J. D., Evans, R. A., Niemczuk, J., and Ross P., *Active Twist Smart Rotor Technology for Blade-Vortex Interaction Noise Reduction*, Proc. SPIE 3668, 37, 1999.
- [23]Sitaraman, J., Baeder, J. B., *Enhanced Unsteady Airload Models Using CFD*, AIAA Paper 2000-2465, Denver, CO, USA, June, 2000.
- [24]Lim, J. W., van der Wall, B. G., *Investigation of the Effect of a Multiple Trailer Wake Model for Descending Flights*, Presented at the 61th Forum of the American Helicopter Society, Grapevine, TX, USA, June 2005.
- [25]Lim, J.W., *The Effect of Fuselage and Rotor Hub on Blade-Vortex Interactions Airloads and Rotor Wakes*, Presented at the 36th European Rotorcraft Forum, Paris, France, Sept. 2010.
- [26]Sa, J. H., You, Y.-H., Park, J.-S., Jung, S.N., Park, S. H., and Yu, Y. H., *Assessment of CFD/CSD Coupled Aeroelastic Analysis Solution for HART II Rotor Incorporating Fuselage Effects*, Presented at the 67th Forum of the American Helicopter Society, Virginia Beach, VA, USA, May 2011.
- [27]Biedron, R. T., Lee-Rausch, E. M., *An Examination of Unsteady Airloads on a UH-60A Rotor: Computation versus Measurement*, Presented at the 68th Forum of the American Helicopter Society, Fort Worth, TX, USA, May 2012.
- [28]Park, J.-S., You, Y.-H., Sa, J. H., Park, S. H., and Jung, S.N., *Extensive Validation of CFD/CSD Aeroelastic Simulations for a Helicopter in Descending Flight*, Presented at the 68th Forum of the American Helicopter Society, Fort Worth, TX, USA, May 2012.

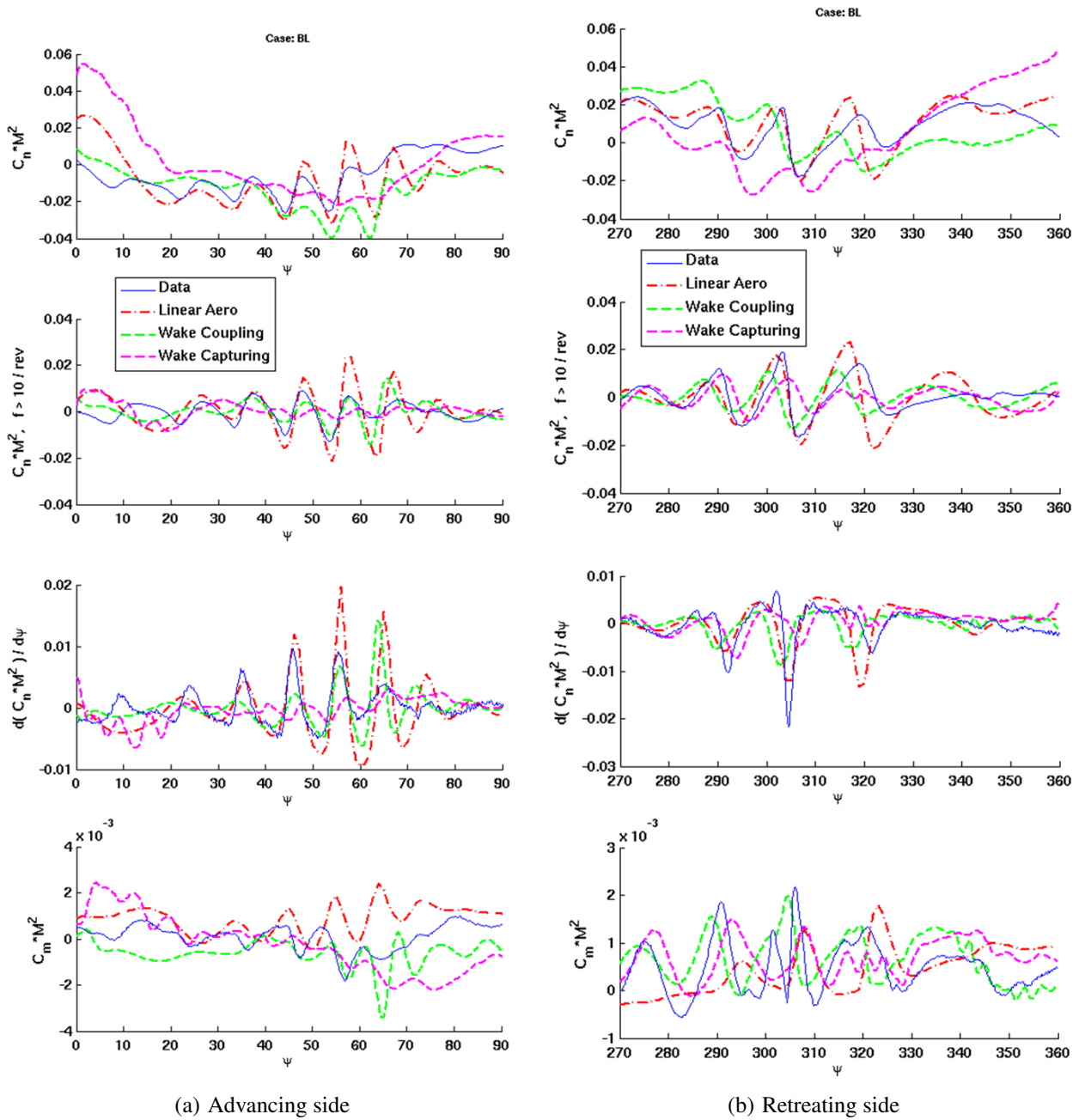


Fig. 15: Normal force and pitching moment, unfiltered, 10/rev filtered, time derivatives, BL case.

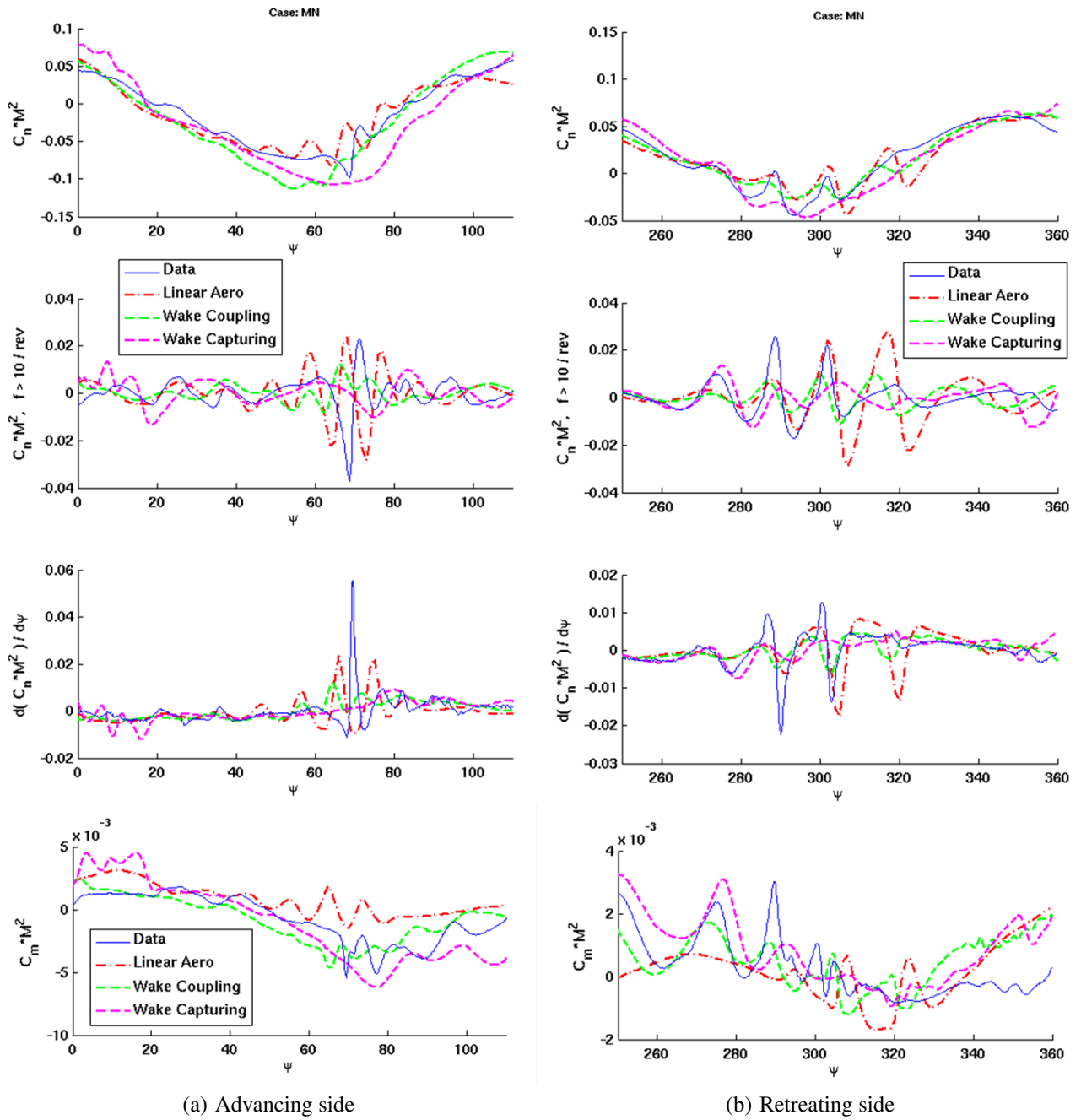
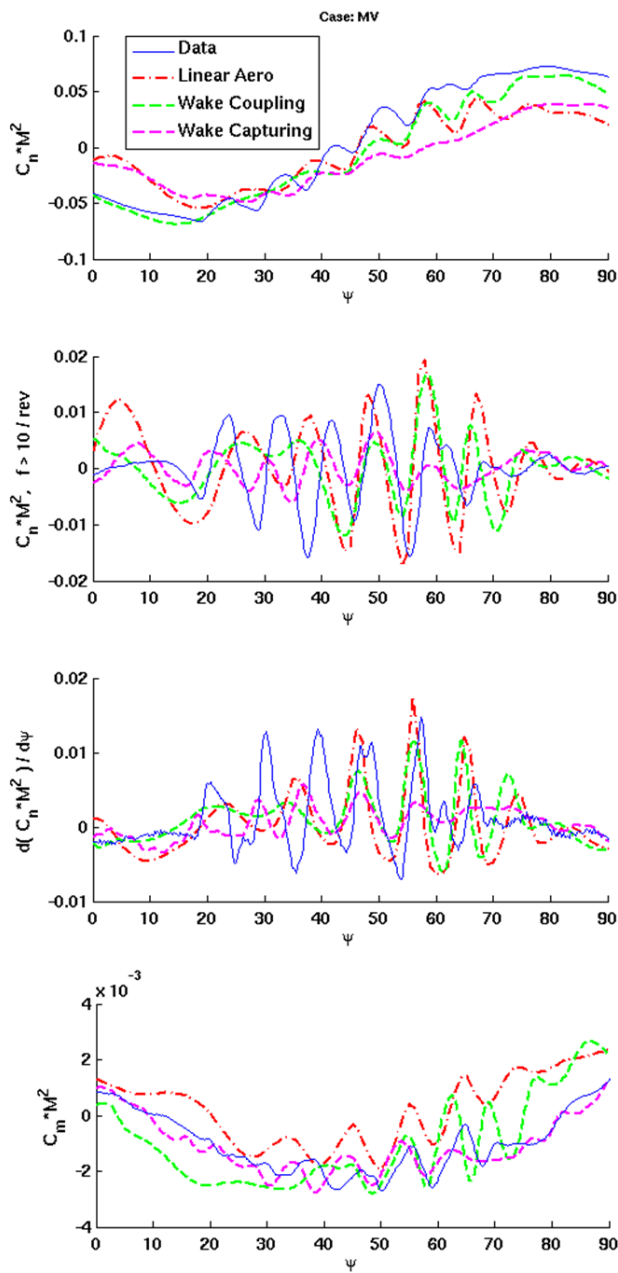
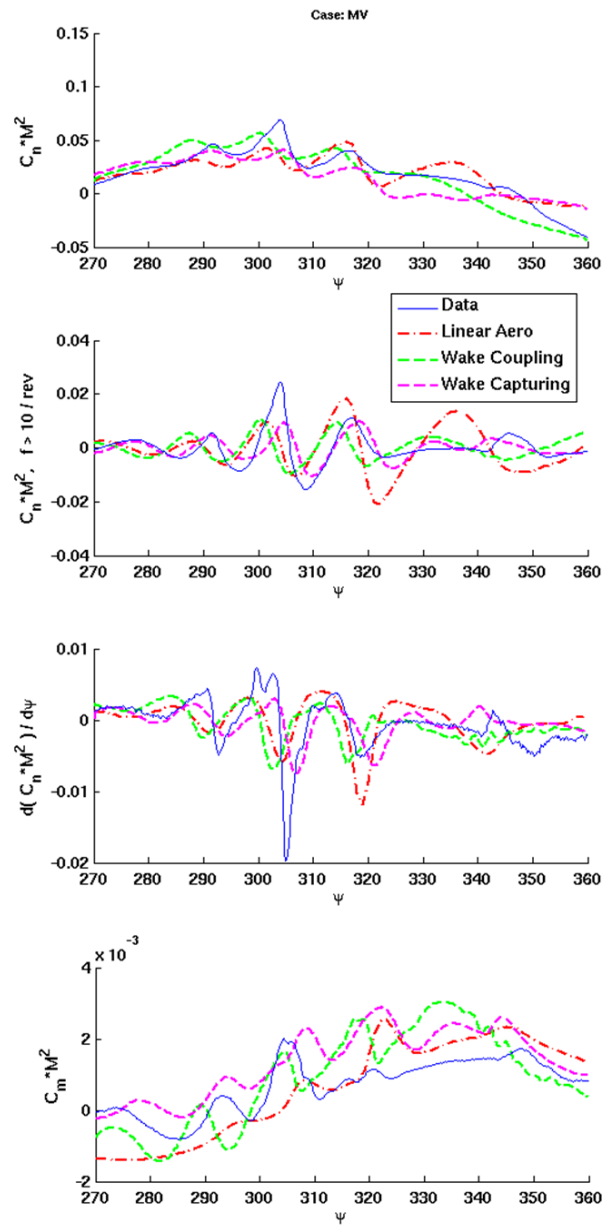


Fig. 16: Normal force and pitching moment, unfiltered, 10/rev filtered, time derivatives, MN case.

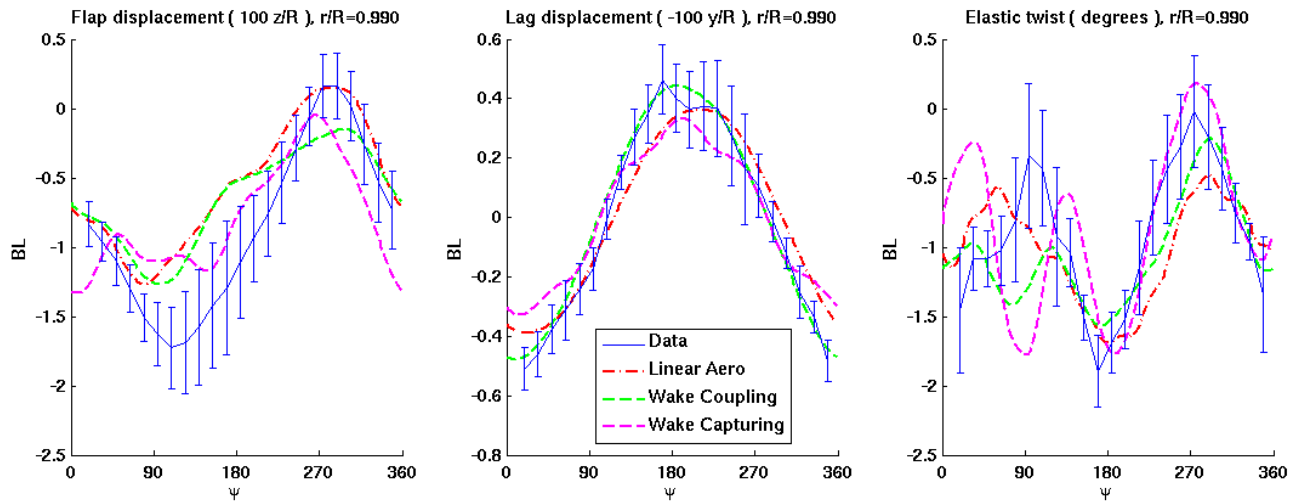


(a) Advancing side

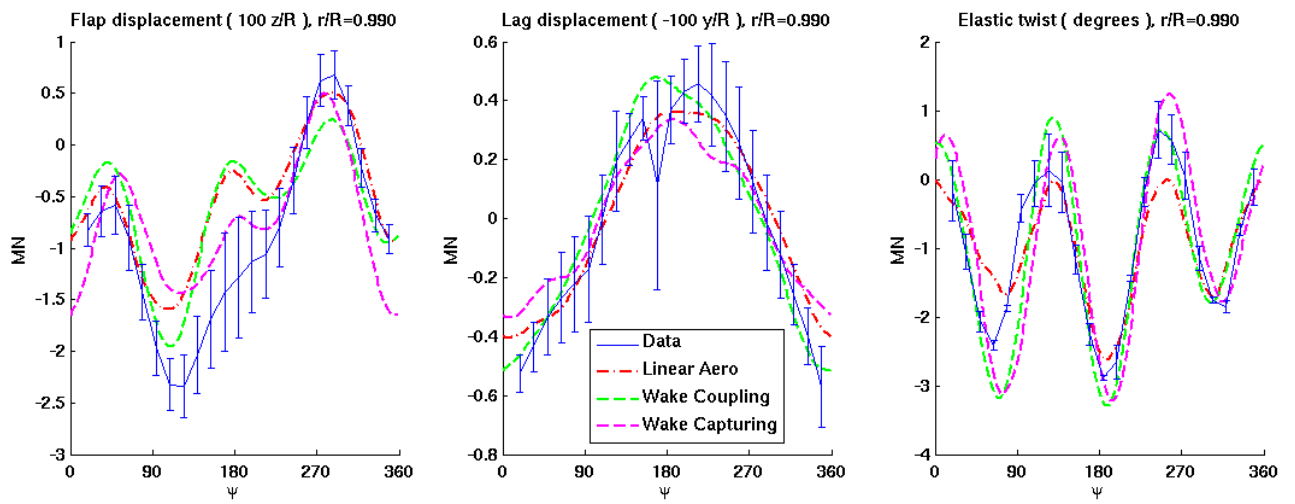


(b) Retreating side

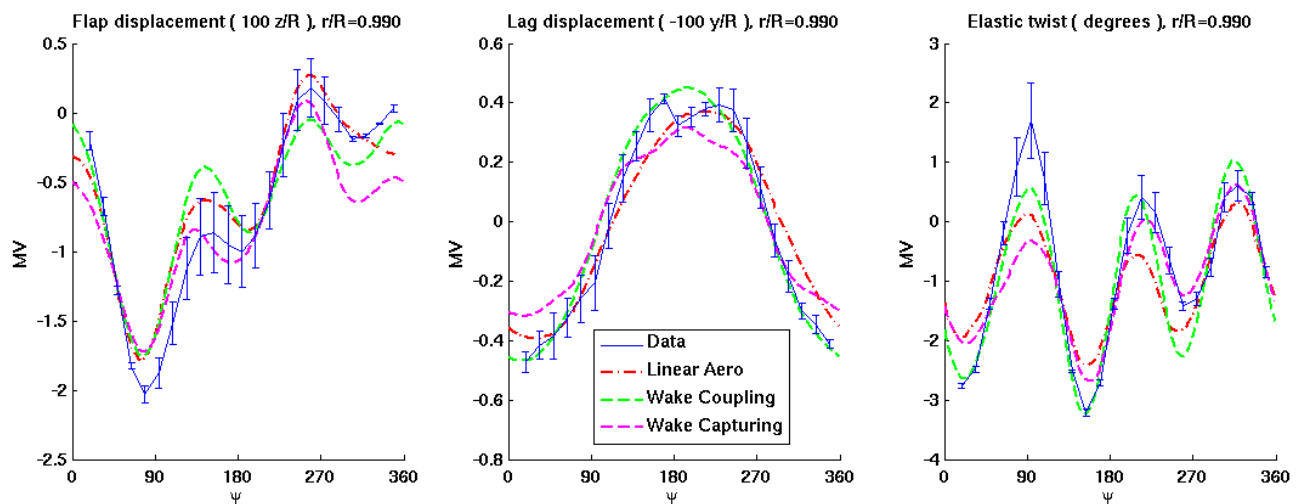
Fig. 17: Normal force and pitching moment, unfiltered, 10/rev filtered, time derivatives, MV case.



(a) Baseline case



(b) Minimum Noise case



(c) Minimum Vibration case

Fig. 18: Blade elastic flap, lead-lag, and torsion displacements.

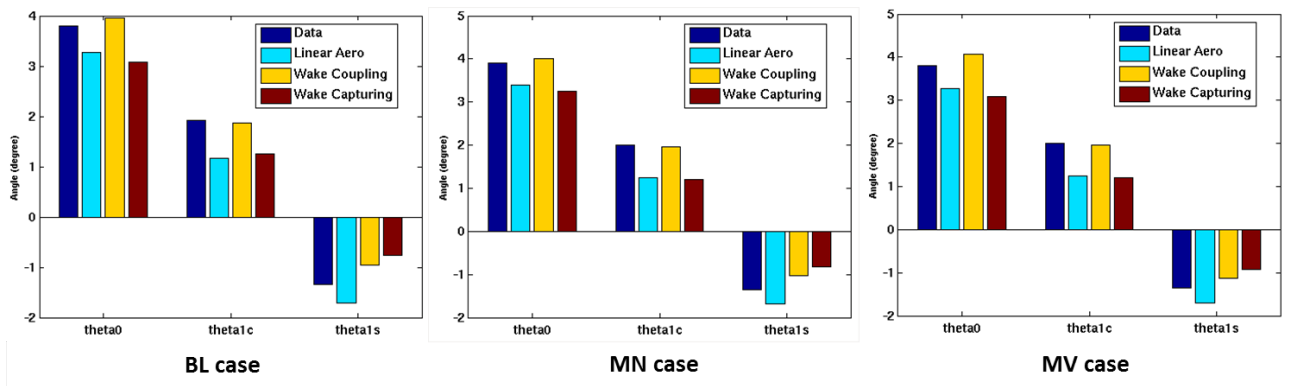


Fig. 19: Trimmed control angles (θ_0 , θ_{1c} , θ_{1s}) for the three cases.

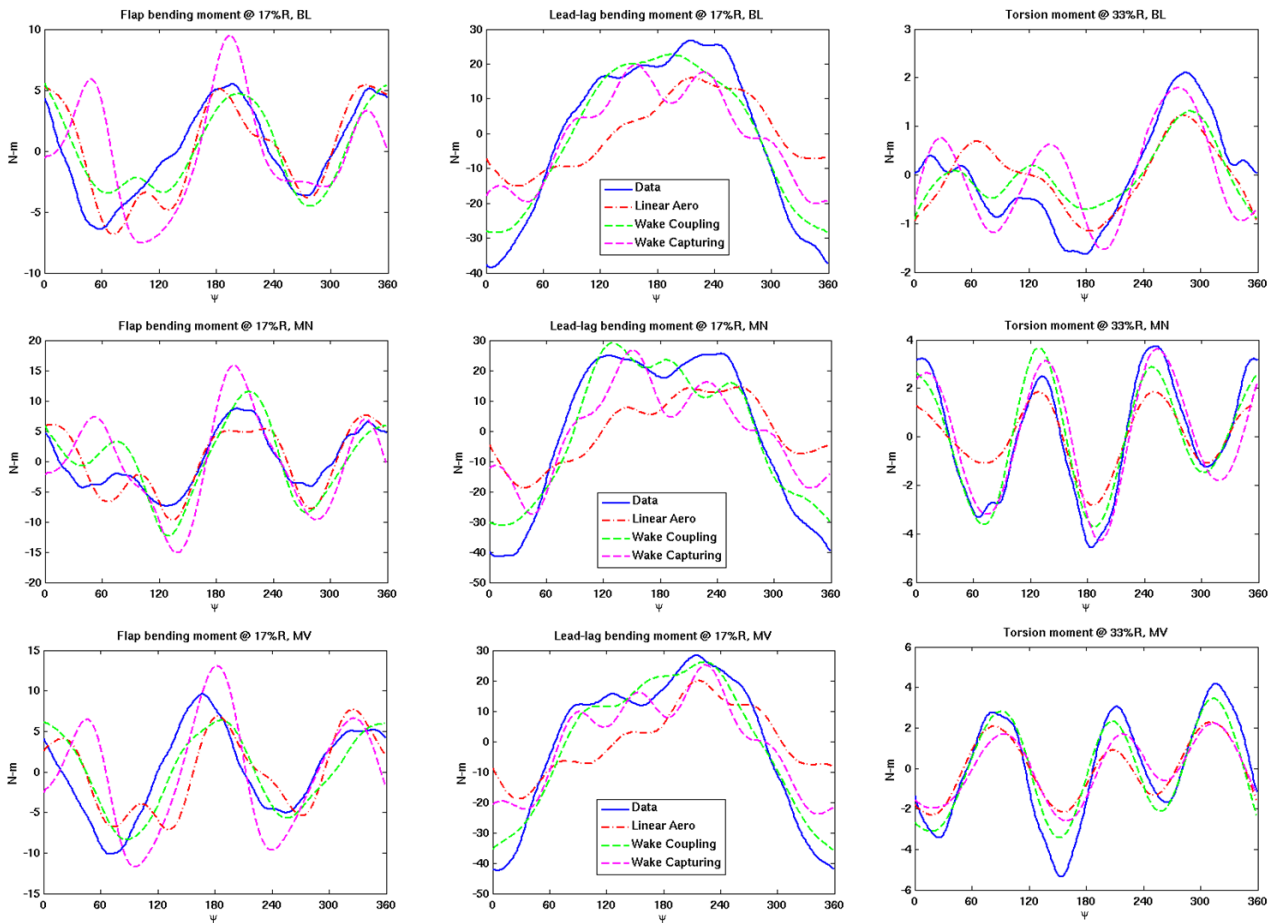
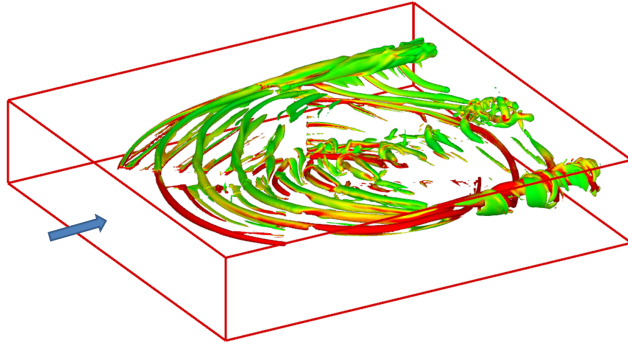
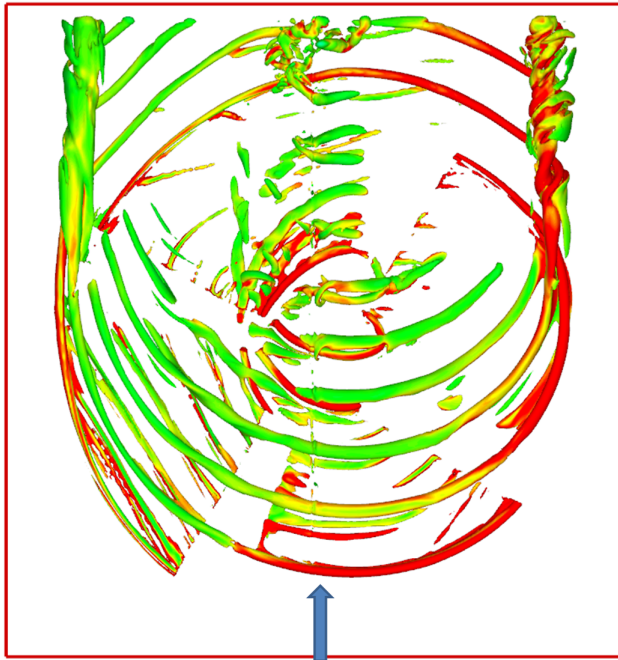


Fig. 20: Blade structural moments, flap lead-lag, torsion.



(a) Iso view



(b) Top view

Fig. 21: Iso-surfaces of Q-criterion colored by vorticity magnitude (levels: 0.03-0.15), MV case, reference blade at 70° (blade solutions not shown).

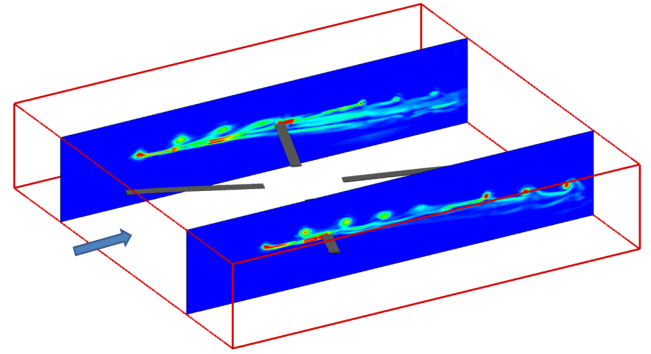
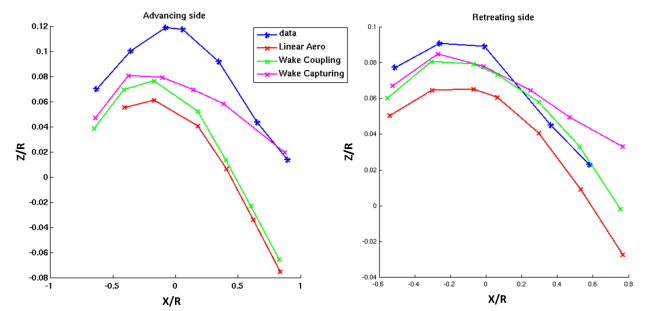
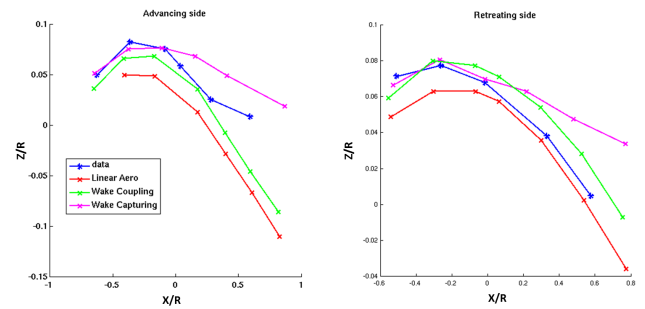


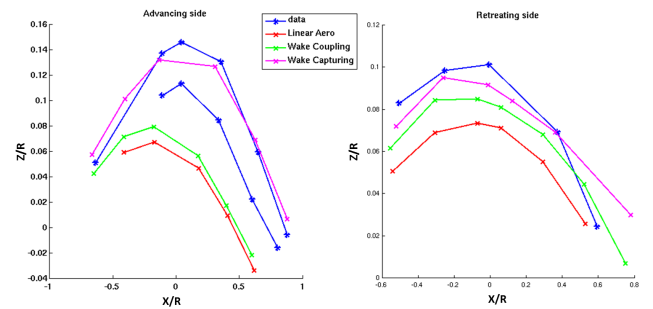
Fig. 22: Planes where wake geometry is compared (vorticity magnitude levels: 0.01-0.15), MV case, reference blade at 70°).



(a) Baseline case



(b) Minimum Noise case



(c) Minimum Vibration case

Fig. 23: Vortex vertical position comparison on the advancing and retreating sides.

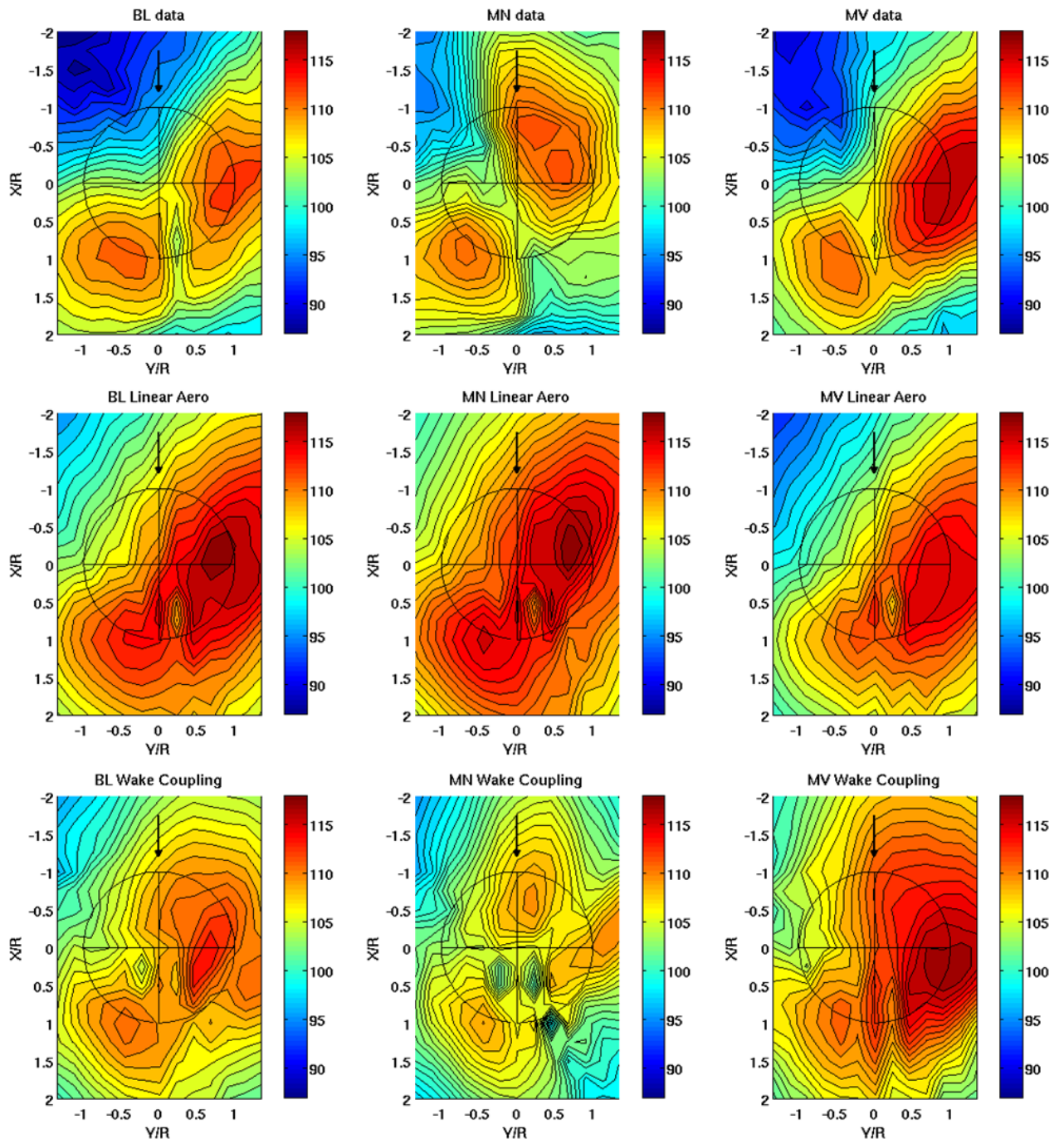


Fig. 24: BVISPL contours (6-40 BPF).